Optimal maneuver strategy to improve the observability of angles-only rendezvous

DU Ronghua, LIAO Wenhe[*], and ZHANG Xiang

School of Mechanical Engineering, Nanjing University of Science and Technology, Nanjing 210094, China

Abstract: This paper proposes an optimal maneuver strategy to improve the observability of angles-only rendezvous from the perspective of relative navigation. A set of dimensionless relative orbital elements (ROEs) is used to parameterize the relative motion, and the objective function of the observability of angles-only navigation is established. An analytical solution of the optimal maneuver strategy to improve the observability of angles-only navigation is obtained by means of numerical analysis. A set of dedicated semi-physical simulation system is built to test the performances of the proposed optimal maneuver strategy. Finally, the effectiveness of the method proposed in this paper is verified through the comparative analysis of the objective function of the observability of angles-only navigation and the performances of the angles-only navigation filter under different maneuver schemes. Compared with the cases without orbital maneuver, it is concluded that the tangential filtering accuracy with the optimal orbital maneuver at the terminal time is increased by 35% on average, and the radial and normal filtering accuracy is increased by 30% on average.

Keywords: angles-only navigation, observability, optimal maneuver, orbital rendezvous.

1. Introduction

With the continuous development of aerospace technology, the scope of aerospace missions is no longer limited to traditional applications (e.g., communication, navigation, and remote sensing). Other aerospace missions including on-orbit servicing [1,2], space debris removal [3,4], formation flying [5,6], and deep space exploration [7,8] are under rapid development. These aerospace missions all involve rendezvous and proximity operations of spacecraft, and the related technologies have also become international research hotspots.

In order to ensure the successful execution of aerospace missions such as on-orbit servicing and space debris removal, it is urgent to improve the automated capabilities of spacecraft (e.g., automated detection and tracking, automated relative navigation, and automated relative trajectory planning and control). This paper focuses on the research of automated relative navigation methods which the chaser spacecraft can autonomously acquire the relative motion state through the relative navigation sensors. The active sensors (e.g., LiDAR and microwave radar) are commonly used to measure the relative motion state between two spacecraft. However, due to their high power consumption and mass, they cannot be used on the micro-satellite platforms. The passive sensors (e.g., optical and infrared cameras) have many advantages [9−11] because they are employable at various inter-satellite separation ranges with little impact on the design of the mass/power of the chaser spacecraft. In addition, most spacecraft are equipped with onboard cameras. If the direction is appropriate, these onboard cameras can be used to capture the space targets within field of view and perform angles-only navigation operations. This so-called angles-only navigation provides a passive, robust, and high-dynamic-range capability. Accordingly, angles-only navigation represents a critical enabling technology for a variety of advanced distributed space system missions, including autonomous rendezvous and docking, space situational awareness, advanced distributed aperture science, and on-orbit servicing of non-cooperative spacecraft [12].

A particular application case of angles-only navigation consists in employing a monocular camera to rendezvous in space with a non-cooperative target. However, the angles-only navigation system suffers from a relative range observability problem during near-range rendezvous [13]. Many scholars have studied the methods to improve the observability of the angles-only navigation system. The first method consists in performing maneu-

ver operations [14,15]. The second method consists in introducing a camera offset with respect to the center of mass of the chaser spacecraft [16]. The third method is to improve the modeling of the relative dynamics and measurement equations to improve the maneuver-free observability of angles-only navigation [17,18]. However, the second method is only suitable for a close range. The third method is sensitive to the measurement noise of the relative navigation sensors, as well as requiring high-precision modeling of the relative dynamics and measurement equations.

To address the problems of the above methods, this paper proposes an optimal maneuver strategy to improve the observability of angles-only rendezvous. First of all, this paper describes the reason why angles-only navigation is not observable. Then, a set of dimensionless relative orbital elements (ROEs) is used to parameterize the relative motion, and then a set of relative dynamics model based on ROEs is established. Compared with the Clohessy-Wiltshire (CW) equation, the relative dynamics model based on ROEs can incorporate various perturbations and can intuitively display the geometric shape of relative motion. Then, a model of observability analysis of angles-only navigation is introduced, and an objective function for observability analysis of angles-only navigation is established. The conditions for achieving the optimal observability of angles-only navigation are analyzed, and the analytical solution of the optimal maneuver strategy is obtained by means of numerical analysis. In addition, a set of dedicated semi-physical simulation system is built to verify the optimal maneuver strategy proposed in this paper. Finally, the optimal maneuver strategy proposed in this paper is verified through the comparative analysis of the objective function of the observability of angles-only navigation and the performances of the angles-only navigation filter under different maneuver schemes.

2. Problem description

The purpose of angles-only navigation is to derive the relative motion state between the space target and the chaser spacecraft, and the relative motion state corresponds to a set of line-of-sight (LoS) measurements $\{\boldsymbol{u}_i, i = 1, 2, \cdots, k\}$. In general, the problem of angles-only navigation is closely related to the observability of the system. Woffinden et al. [19] prove that the relative motion state is not observable under the assumption of an homogeneous linear relative motion with a linear measurement model.

First, let $\boldsymbol{x}(t)$ denote the relative motion state between the space target and the chaser spacecraft at time t, then the propagation equation of the relative motion state can

be expressed as

$$\boldsymbol{x}(t) = \boldsymbol{\Phi}(t, t_0)\boldsymbol{x}(t_0) \qquad (1)$$

where $\boldsymbol{\Phi}(t, t_0)$ is the state transfer matrix (STM) between the initial epoch t_0 and time t.

Assume that there is a linear correlation between the relative position vector $\boldsymbol{r}(t)$ and relative motion state $\boldsymbol{x}(t)$, which can be expressed as

$$\boldsymbol{r}(t) = \boldsymbol{C}(t)\boldsymbol{x}(t). \qquad (2)$$

A set of LoS measurements $\{\boldsymbol{u}_i, i = 1, 2, \cdots, k\}$ and the relative position vector $\boldsymbol{r}(t)$ satisfy

$$\boldsymbol{u}_i \cdots \boldsymbol{r}(t_i) = \boldsymbol{0}, \ \ i \in [1, k]. \qquad (3)$$

Substituting (1) and (2) into (3) yields:

$$\boldsymbol{u}_i \cdots (\boldsymbol{C}(t_i)\boldsymbol{\Phi}(t_i, t_0)\boldsymbol{x}(t_0)) = \boldsymbol{0}, \ \ i \in [1, k]. \qquad (4)$$

It can be seen from (4) that if $\boldsymbol{x}(t_0) = \boldsymbol{x}_0$ is the solution of (4), the scaled solution $\phi\boldsymbol{x}_0$ (ϕ is the scale factor) is also the solution of (4), resulting in infinite solutions matching the set of LoS measurements $\{\boldsymbol{u}_i, i = 1, 2, \cdots, k\}$, and this is known as Woffinden's dilemma [20].

3. Mathematical basis

3.1 Relative dynamics model

The CW equation is commonly used to establish the spacecraft relative dynamics model. However, the CW equation is only suitable for the orbital scenarios where the inter-satellite separation range is small and various perturbations are ignored. The spacecraft relative dynamics model established based on ROEs can consider the effects of various perturbations, as well as the geometry of the relative trajectory can be displayed intuitively.

Ignoring the second-order terms of the spacecraft relative dynamics model established based on ROEs, a linear dynamics model is obtained, which is still effective in the presence of various perturbations. The closed-form solution of the mean ROEs over the time interval $[t_0, t_f]$ [21] has the following form:

$$\delta\boldsymbol{\alpha}(t_f) = \boldsymbol{\Phi}(t_f, t_0)\delta\boldsymbol{\alpha}(t_0) + \sum_{k=1}^{p} \boldsymbol{\Phi}(t_f, t_k)\boldsymbol{\Gamma}_k\delta\boldsymbol{v}_k \qquad (5)$$

where $\{\boldsymbol{\Gamma}_k, \ k = 1, 2, \cdots, p\}$ denotes the control-input matrix, $\delta\boldsymbol{v} = (\delta v_R, \delta v_T, \delta v_N)^{\mathrm{T}}$ denotes the impulse maneuver depicted in the local Cartesian orbital frame of the chaser spacecraft.

The adoption of impulsive $\delta\boldsymbol{v}$ implies the maneuvers with short duration, which will cause an instantaneous change in the velocity of the chaser spacecraft without changing the position. The parameterized form of the mean ROEs used in this paper [22] is expressed as

$$\delta\boldsymbol{\alpha} = \begin{bmatrix} \delta a \\ \delta\lambda \\ \delta e_x \\ \delta e_y \\ \delta i_x \\ \delta i_y \end{bmatrix} = \begin{bmatrix} (a_d - a_c)/a_c \\ u_d - u_c + (\Omega_d - \Omega_c)\cos i_c \\ e_d\cos\omega_d - e_c\cos\omega_c \\ e_d\sin\omega_d - e_c\sin\omega_c \\ i_d - i_c \\ (\Omega_d - \Omega_c)\sin i_c \end{bmatrix} \qquad (6)$$

where a, e, i, Ω, ω, and M are the Kepler orbit elements, δa denotes the relative semimajor axis, $\delta\lambda$ denotes the relative mean longitude, $\delta\boldsymbol{e} = (\delta e_x, \delta e_y)^{\mathrm{T}}$ denotes the relative eccentricity vector, $\delta\boldsymbol{i} = (\delta i_x, \delta i_y)^{\mathrm{T}}$ denotes the relative inclination vector, and $u = M + \omega$ denotes the mean argument of latitude.

Compared with the relative motion state depicted in the local Cartesian orbital frame (i.e., radial, tangential (along-track), and normal (cross-track)), the relative dynamics model using ROEs has the advantages of providing a quick insight into the geometry of the relative trajectory. Fig. 1 describes the relative motion depicted in the local Cartesian orbital frame, whose the unit vector is defined as follows: $\boldsymbol{e}_R$ and $\boldsymbol{e}_N$ are aligned with the absolute position and the orbital angular momentum of the chaser spacecraft, and $\boldsymbol{e}_T$, $\boldsymbol{e}_R$ and $\boldsymbol{e}_N$ satisfy the right-hand rule. In addition, it can be seen from Fig. 1, the size of the relative motion can be depicted by the means of the dimensioned (i.e., scaled with the semi-major axis a) ROEs [20].
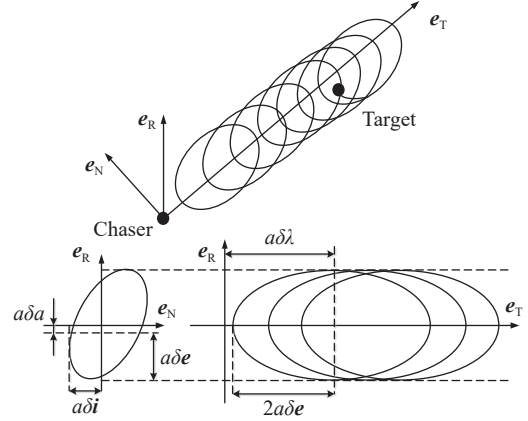

Fig. 1   Relative motion parameterization

The set of ROEs is particularly suitable for the problem of angles-only navigation because the weakly observable inter-satellite range is almost equal to the component $a\delta\lambda$. The relative dynamics model established based on ROEs is effective for circular orbits ($e_c = 0$), but it is still singular for equatorial orbits ($i_c = 0$) [23]. For orbits with arbitrary eccentricity, the STM defined by the mean ROEs including J_2 perturbations, atmospheric drag, solar radiation pressure, and third body gravity is obtained. In the case of only J_2 perturbations, the STM over the time interval $[t_0, t_f]$ [24] is expressed as

$$\boldsymbol{\Phi}(t_f, t_0) = \begin{bmatrix} 1 & 0 & 0 & 0 & 0 & 0 \\ -\frac{7}{2}\kappa EP\tau - \frac{3}{2}n\tau & 1 & \kappa e_{x0}FGP\tau & \kappa e_{y0}FGP\tau & -\kappa FS\tau & 0 \\ \frac{7}{2}\kappa e_{yf}Q\tau & 0 & \cos(\dot\omega\tau) - 4\kappa e_{x0}e_{yf}GQ\tau & -\sin(\dot\omega\tau) - 4\kappa e_{y0}e_{yf}GQ\tau & 5\kappa e_{yf}S\tau & 0 \\ -\frac{7}{2}\kappa e_{xf}Q\tau & 0 & \sin(\dot\omega\tau) + 4\kappa e_{x0}e_{xf}GQ\tau & \cos(\dot\omega\tau) + 4\kappa e_{y0}e_{xf}GQ\tau & -5\kappa e_{xf}S\tau & 0 \\ 0 & 0 & 0 & 0 & 1 & 0 \\ \frac{7}{2}\kappa S\tau & 0 & -4\kappa e_{x0}GS\tau & -4\kappa e_{y0}GS\tau & 2\kappa T\tau & 1 \end{bmatrix} \qquad (7)$$

where

$$\begin{cases} \gamma = \dfrac{3}{4}J_2 R_e^2\sqrt{\mu} \\ \eta = \sqrt{1 - \|\boldsymbol{e}\|^2} \\ \kappa = \dfrac{\gamma}{a^{7/2}\eta^4} \\ G = \dfrac{1}{\eta^2} \\ E = 1 + \eta \\ F = 4 + 3\eta \\ T = \sin^2 i \\ \tau = t_f - t_0 \\ P = 3\cos^2 i - 1 \\ Q = 5\cos^2 i - 1 \\ S = \sin(2i) \\ \dot\omega = \kappa Q \end{cases}, \qquad (8)$$

where the subscripts 0 and f represent the initial and final values of the orbital elements of the chaser spacecraft, respectively, e_x and e_y are the x and y components of the absolute eccentricity vector $\boldsymbol{e}$, μ is the Earth's gravitational constant, R_e is the Earth's equator radius, and n is the mean motion of the chaser spacecraft.

The change in the ROEs caused by the impulse maneuver of the chaser spacecraft is expressed as

$$\Delta\delta\boldsymbol{\alpha}_k = \boldsymbol{\Gamma}_k\delta\boldsymbol{v}_k \qquad (9)$$

where Δ represents the arithmetic difference of the ROEs before and after the impulse maneuver.

For the orbital scenarios where the chaser spacecraft is in a near-circular orbit (i.e., $e_c = 0$), the STM given by (7) [25] can be simplified as

$$\boldsymbol{\Phi}(t_f, t_0) = \begin{bmatrix} 1 & 0 & 0 & 0 & 0 & 0 \\ -\dfrac{7\kappa EP + 3n}{2}\tau & 1 & 0 & 0 & -\kappa FS\tau & 0 \\ 0 & 0 & \cos(\dot{\omega}\tau) & -\sin(\dot{\omega}\tau) & 0 & 0 \\ 0 & 0 & \sin(\dot{\omega}\tau) & \cos(\dot{\omega}\tau) & 0 & 0 \\ 0 & 0 & 0 & 0 & 1 & 0 \\ \dfrac{7}{2}\kappa S\tau & 0 & 0 & 0 & 2\kappa T\tau & 1 \end{bmatrix}. \tag{10}$$

The argument of latitude u of the chaser spacecraft is used as the independent variable instead of time, and τ in (10) can be expressed [23] as

$$\tau = \frac{\Delta u}{n + \kappa(\eta P + Q)} \tag{11}$$

where Δu is the change in the argument of latitude of the chaser spacecraft over the time interval $[t_0, t_f]$.

The effects of an impulse maneuver executed at the mean argument of latitude u_k are given by (7) for near-circular orbits can be expressed [26] as

$$\Delta\delta\boldsymbol{\alpha}_k = \boldsymbol{\Gamma}_k \delta\boldsymbol{v}_k =$$
$$\frac{1}{na} \begin{bmatrix} 0 & 2 & 0 \\ -2 & 0 & 0 \\ \sin u_k & 2\cos u_k & 0 \\ -\cos u_k & 2\sin u_k & 0 \\ 0 & 0 & \cos u_k \\ 0 & 0 & \sin u_k \end{bmatrix} \begin{bmatrix} \delta v_R \\ \delta v_T \\ \delta v_N \end{bmatrix}. \tag{12}$$

Equation (12) shows that the effects of the impulse maneuvers which are in and out of the orbital plane are decoupled.

3.2 Measurement model

The general form of the nonlinear measurement model is obtained as

$$\boldsymbol{z} = \boldsymbol{h}(\boldsymbol{x}, t). \tag{13}$$

The camera frame needs to be defined before defining the LoS measurements. Without loss of generality, it is assumed that the optical axis of the camera is aligned with the opposite direction of flight. Under this assumption, the relationship between the relative position vectors depicted in the camera frame and the local Cartesian orbital frame is given as

$$\boldsymbol{r}_{rel} = \boldsymbol{R}_{RTN}^c \boldsymbol{r}^{RTN} = \begin{bmatrix} 1 & 0 & 0 \\ 0 & 0 & 1 \\ 0 & -1 & 0 \end{bmatrix} \boldsymbol{r}^{RTN}. \tag{14}$$

The azimuth α and elevation ϵ can be expressed as a function of the relative position vector $\boldsymbol{r}_{rel} = (r_x^c, r_y^c, r_z^c)^T$ depicted in the camera frame, as shown in Fig. 2, which can be expressed as

$$\boldsymbol{z} = \begin{pmatrix} \alpha \\ \varepsilon \end{pmatrix} = \begin{pmatrix} \arcsin\left(\dfrac{r_y^c}{\|\boldsymbol{r}_{rel}\|}\right) \\ \arctan\left(\dfrac{r_x^c}{r_z^c}\right) \end{pmatrix}. \tag{15}$$
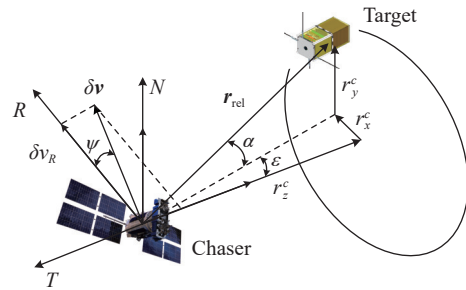

Fig. 2 LoS measurement geometry

4. Analytical solution of optimal maneuver strategy

According to the theory proposed by Jonathan Grzymisch and Walter Fichter, in order to maximize the observability of angles-only navigation, the following objective function should be minimized [27]:

$$J = \bar{\boldsymbol{x}}_{rel}^T \boldsymbol{x}_{rel} \tag{16}$$

where $\bar{\boldsymbol{x}}_{rel}$ is the relative trajectory between the chaser spacecraft and the space target without the impulse maneuver, and $\boldsymbol{x}_{rel}$ is the relative trajectory between the chaser spacecraft and the space target after the impulse maneuver, namely

$$\bar{\boldsymbol{x}}_{rel}(t_f) = a\boldsymbol{C}(t_f)\boldsymbol{\Phi}(t_f, t_0)\delta\boldsymbol{\alpha}(t_0), \tag{17}$$

$$\boldsymbol{x}_{rel}(t_f) = a\boldsymbol{C}(t_f)\left(\boldsymbol{\Phi}(t_f, t_0)\delta\boldsymbol{\alpha}(t_0) + \sum_{k=1}^{p}\boldsymbol{\Phi}(t_f, t_k)\boldsymbol{\Gamma}_k\delta\boldsymbol{v}_k\right), \tag{18}$$

where $\delta\boldsymbol{\alpha}(t_0) = \delta\boldsymbol{\alpha}_0$ is the initial ROEs, and $\boldsymbol{C}$ is the transformation matrix between the ROEs and the relative position vectors depicted in the local Cartesian orbital frame.

The concept of the observability angle proposed by Woffinden et al. [19] can also be used to define the objective function of the observability of angles-only navigation after the impulse maneuver:

$$\theta = \arccos\left(\frac{\bar{\boldsymbol{x}}_{rel} \cdot \boldsymbol{x}_{rel}}{\|\bar{\boldsymbol{x}}_{rel}\|\|\boldsymbol{x}_{rel}\|}\right). \tag{19}$$

The geometrical schematic diagram of the observability angle θ is shown in Fig. 3.
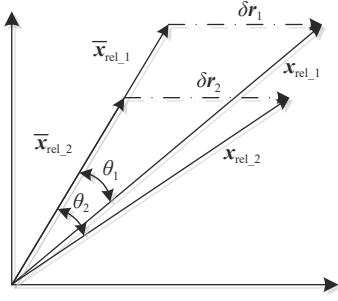

Fig. 3   Definition of observability angle θ

When the absolute value the observability angle θ is equal to $\pi/2$, the observability of angles-only navigation is optimal [19]. δr is the change in the relative position vectors between the chaser spacecraft and the space target after the impulse maneuver, which can be expressed as

$$\delta \boldsymbol{r} = a\boldsymbol{C}(t_f)\left(\sum_{k=1}^{p}\boldsymbol{\Phi}(t_f,t_k)\boldsymbol{\Gamma}_k\delta\boldsymbol{v}_k\right). \tag{20}$$

For the unobservable impulse maneuver, the relative trajectory $\boldsymbol{x}_{\mathrm{rel}}$ after the impulse maneuver and the relative trajectory $\bar{\boldsymbol{x}}_{\mathrm{rel}}$ without the impulse maneuver satisfy a positive linear relationship [28], that is, the observation angle $\theta = 0°$, or

$$\chi\left(\boldsymbol{C}(t_f)\boldsymbol{\Phi}(t_f,t_0)\delta\boldsymbol{\alpha}(t_0)\right) =$$
$$\boldsymbol{C}(t_f)\left(\boldsymbol{\Phi}(t_f,t_0)\delta\boldsymbol{\alpha}(t_0) + \sum_{k=1}^{p}\boldsymbol{\Phi}(t_f,t_k)\boldsymbol{\Gamma}_k\delta\boldsymbol{v}_k\right), \ \chi > 0. \tag{21}$$

Equation (21) means that when the relative trajectory $\boldsymbol{x}_{\mathrm{rel}}$ after the impulse maneuver and the relative trajectory $\bar{\boldsymbol{x}}_{\mathrm{rel}}$ without the impulse maneuver point in the same direction, the angles-only navigation system after the impulse maneuver is not observable. The sufficient condition that the angles-only navigation system is observable after the impulse maneuver can be expressed as

$$\chi\left(\boldsymbol{C}(t_f)\boldsymbol{\Phi}(t_f,t_0)\delta\boldsymbol{\alpha}(t_0)\right) \neq$$
$$\boldsymbol{C}(t_f)\left(\boldsymbol{\Phi}(t_f,t_0)\delta\boldsymbol{\alpha}(t_0) + \sum_{k=1}^{p}\boldsymbol{\Phi}(t_f,t_k)\boldsymbol{\Gamma}_k\delta\boldsymbol{v}_k\right), \ \chi > 0. \tag{22}$$

Combine the same part $\boldsymbol{C}(t_f)\boldsymbol{\Phi}(t_f,t_0)\cdot \delta\boldsymbol{\alpha}(t_0)$ of (21) to get

$$(\chi-1)\left(\boldsymbol{C}(t_f)\boldsymbol{\Phi}(t_f,t_0)\delta\boldsymbol{\alpha}(t_0)\right) =$$
$$\boldsymbol{C}(t_f)\cdot\sum_{k=1}^{p}\boldsymbol{\Phi}(t_f,t_k)\boldsymbol{\Gamma}_k\delta\boldsymbol{v}_k, \ \chi > 0. \tag{23}$$

And then get

$$\chi'\left(\boldsymbol{C}(t_f)\boldsymbol{\Phi}(t_f,t_0)\delta\boldsymbol{\alpha}(t_0)\right) =$$
$$\boldsymbol{C}(t_f)\cdot\sum_{k=1}^{p}\boldsymbol{\Phi}(t_f,t_k)\boldsymbol{\Gamma}_k\delta\boldsymbol{v}_k, \ \chi' > -1 \tag{24}$$

where $\chi' = \chi - 1$.

For $\chi' > -1$, multiply both sides of the inequality by $\boldsymbol{C}(t_f)\boldsymbol{\Phi}(t_f,t_0)\delta\boldsymbol{\alpha}(t_0)$ to get

$$\chi'\boldsymbol{C}(t_f)\boldsymbol{\Phi}(t_f,t_0)\delta\boldsymbol{\alpha}(t_0) > -\boldsymbol{C}(t_f)\boldsymbol{\Phi}(t_f,t_0)\delta\boldsymbol{\alpha}(t_0),$$
$$\boldsymbol{C}(t_f)\boldsymbol{\Phi}(t_f,t_0)\delta\boldsymbol{\alpha}(t_0) > \boldsymbol{0}, \tag{25}$$

$$\chi'\boldsymbol{C}(t_f)\boldsymbol{\Phi}(t_f,t_0)\delta\boldsymbol{\alpha}(t_0) < -\boldsymbol{C}(t_f)\boldsymbol{\Phi}(t_f,t_0)\delta\boldsymbol{\alpha}(t_0),$$
$$\boldsymbol{C}(t_f)\boldsymbol{\Phi}(t_f,t_0)\delta\boldsymbol{\alpha}(t_0) < \boldsymbol{0}. \tag{26}$$

According to the relationship depicted in (24), inequalities (25) and (26) can be re-expressed as

$$\boldsymbol{C}(t_f)\left(\sum_{k=1}^{p}\boldsymbol{\Phi}(t_f,t_k)\boldsymbol{\Gamma}_k\delta\boldsymbol{v}_k\right) > -\boldsymbol{C}(t_f)\boldsymbol{\Phi}(t_f,t_0)\delta\boldsymbol{\alpha}(t_0),$$
$$\boldsymbol{C}(t_f)\boldsymbol{\Phi}(t_f,t_0)\delta\boldsymbol{\alpha}(t_0) > \boldsymbol{0}, \tag{27}$$

$$\boldsymbol{C}(t_f)\left(\sum_{k=1}^{p}\boldsymbol{\Phi}(t_f,t_k)\boldsymbol{\Gamma}_k\delta\boldsymbol{v}_k\right) < -\boldsymbol{C}(t_f)\boldsymbol{\Phi}(t_f,t_0)\delta\boldsymbol{\alpha}(t_0),$$
$$\boldsymbol{C}(t_f)\boldsymbol{\Phi}(t_f,t_0)\delta\boldsymbol{\alpha}(t_0) < \boldsymbol{0}. \tag{28}$$

And then get

$$\boldsymbol{C}(t_f)\left(\sum_{k=1}^{p}\boldsymbol{\Phi}(t_f,t_k)\boldsymbol{\Gamma}_k\delta\boldsymbol{v}_k + \boldsymbol{\Phi}(t_f,t_0)\delta\boldsymbol{\alpha}(t_0)\right) > \boldsymbol{0},$$
$$\boldsymbol{C}(t_f)\boldsymbol{\Phi}(t_f,t_0)\delta\boldsymbol{\alpha}(t_0) > \boldsymbol{0}, \tag{29}$$

$$\boldsymbol{C}(t_f)\left(\sum_{k=1}^{p}\boldsymbol{\Phi}(t_f,t_k)\boldsymbol{\Gamma}_k\delta\boldsymbol{v}_k + \boldsymbol{\Phi}(t_f,t_0)\delta\boldsymbol{\alpha}(t_0)\right) < \boldsymbol{0},$$
$$\boldsymbol{C}(t_f)\boldsymbol{\Phi}(t_f,t_0)\delta\boldsymbol{\alpha}(t_0) < \boldsymbol{0}. \tag{30}$$

These constraints indicate that in order to maintain the positive nature of the required linear relationship, the chaser spacecraft should be located on the same side of the space target before and after the impulse maneuver. In order to maximize the observability of angles-only navigation after the impulse maneuver, the value of the objective function J should be minimized, that is, the value of J should be zero, and we can get

$$a^2(\boldsymbol{C}(t_f)\boldsymbol{\Phi}(t_f,t_0)\delta\boldsymbol{\alpha}(t_0))^{\mathrm{T}}\cdot$$
$$\left(\boldsymbol{C}(t_f)\left(\boldsymbol{\Phi}(t_f,t_0)\cdot\delta\boldsymbol{\alpha}(t_0) + \sum_{k=1}^{p}\boldsymbol{\Phi}(t_f,t_k)\boldsymbol{\Gamma}_k\delta\boldsymbol{v}_k\right)\right) = 0. \tag{31}$$

Since it is necessary to determine the optimal maneuver strategy for the observability of angles-only naviga-

tion under certain constraints, it can be depicted by maximizing the linear independence between the relative trajectory x_{rel} after the impulse maneuver and the relative trajectory $\bar{x}_{rel}$ without the impulse maneuver. In order to maximize the observability of angles-only navigation after the impulse maneuver, the objective function can be re-expressed as

$$J(\delta v, \delta \alpha_0, t_f, k) = a^2 (C(t_f)\Phi(t_f, t_0)\delta\alpha(t_0))^{\mathrm{T}} \cdot$$
$$\left(C(t_f)\left(\Phi(t_f, t_0)\delta\alpha(t_0) + \sum_{k=1}^{p}\Phi(t_f, t_k)\Gamma_k\delta v_k\right)\right) \quad (32)$$

where $J(\delta v, \delta \alpha_0, t_f, k) > 0$, and the smaller the J, the better the observability of the angles-only navigation system.

According to (32), the observability of angles-only navigation after a single-impulse maneuver (i.e., $k = 1$) depends on the impulse velocity increment δv, the initial ROEs $\delta\alpha_0$ at the point where the impulse maneuver is performed, and the terminal time t_f. In order to find the impulse maneuver that provides the optimal observability of the angles-only navigation system, that is, the impulse velocity increment δv in (32). Fixing the initial ROEs $\delta\alpha_0$ at the point where the impulse maneuver is performed and the terminal time t_f, and then the impulse velocity increment δv for the optimal observability of the angles-only navigation system can be determined.

Expanding (32), where only one term is a function of the impulse velocity increment δv. For a single-impulse maneuver $\delta v = \delta v_1$, if δv_1 represents the impulse velocity increment of the impulse maneuver at the initial ROEs $\delta\alpha_0$, the minimum objective function J' relative to the impulse velocity increment δv can be expressed as

$$J'(\delta v) = a^2 \Xi^{\mathrm{T}} \aleph \quad (33)$$

where $\Xi = C(t_f)\Phi(t_f, t_0)\delta\alpha(t_0)$ and $\aleph = C(t_f)\Phi(t_f, t_0)\Gamma_1$.

In the actual rendezvous trajectory design process, it is of great significance to find the impulse maneuver within the range of available resources that provides the optimal observability of the angles-only navigation system. In order to find the direction of the optimal maneuver strategy, it is logical to limit the maximum magnitude v of the impulse velocity increment δv. The constraint can be depicted by the following equation:

$$\kappa(\delta v) = v^2 - (\delta v)^{\mathrm{T}}\delta v = 0. \quad (34)$$

The constrained optimization problem becomes a problem of minimizing the objective function in (33) under the impulse velocity increment δv. When the latter constraint does not work, the problem can be transformed into an equivalent unconstrained problem by using the Lagrangian multiplier technique [29]. Accordingly, the problem is reduced to the problem of minimizing the

Lagrangian function

$$\xi(\delta v, \gamma) = J'(\delta v) - \gamma\kappa\delta v \quad (35)$$

where γ is the Lagrangian multiplier corresponding to the constraint in (34).

The first-order optimal Karush-Kuhn-Tucker (KKT) condition is derived from the derivative of the Lagrangian function ξ with respect to the optimization variable δv and the Lagrangian multiplier γ equal to zero [29], namely

$$\frac{\partial\xi}{\partial\gamma} = (\delta v)^{\mathrm{T}}\delta v - v^2 = 0, \quad (36)$$

$$\frac{\partial\xi}{\partial(\delta v)} = a^2\Xi^{\mathrm{T}}\aleph - 2\gamma(\delta v)^{\mathrm{T}} = \mathbf{0}. \quad (37)$$

These equations can be solved for δv and λ to get

$$\gamma = \pm\frac{a^2\sqrt{\Xi^{\mathrm{T}}\aleph\aleph^{\mathrm{T}}\Xi}}{2v}, \quad (38)$$

$$\delta v = \frac{a^2\aleph^{\mathrm{T}}\Xi}{2\gamma}. \quad (39)$$

The second-order optimal KKT conditions provide a constraint on λ to identify which fixed point corresponds to the minimum value of the Lagrangian function ξ, namely

$$\frac{\partial^2\xi}{\partial(\delta v)^2} = -2\gamma. \quad (40)$$

Since the value of (40) needs to be greater than zero, so $\gamma < 0$ is obtained. Finally the algebraic expression of the optimal maneuver $(\delta v)_{obj}$ is obtained as

$$(\delta v)_{obj} = -\frac{v\aleph^{\mathrm{T}}\Xi}{\sqrt{\Xi^{\mathrm{T}}\aleph\aleph^{\mathrm{T}}\Xi}}. \quad (41)$$

This expression is a function of the initial ROEs $\delta\alpha_0$ and the maximum magnitude v of the impulse velocity increment δv, and it provides the optimal observability of the angles-only navigation system at a specific point in time after the impulse maneuver.

Since the impulse maneuvers which are in or out of the orbital plane can be decoupled for analysis [30], this paper separately considers the effects of the impulse maneuvers which are in or out of the orbital plane on the observability of angles-only navigation. For the impulse maneuver which is out of the orbital plane, δv can be expressed as

$$\delta v = \begin{bmatrix} \delta v_R \\ \delta v_T \\ \delta v_N \end{bmatrix} = \begin{bmatrix} 0 \\ 0 \\ \delta v_N \end{bmatrix}. \quad (42)$$

For the impulse maneuver which is in the orbital plane, δv can be expressed as

$$\delta \boldsymbol{v} = \begin{bmatrix} \delta v_R \\ \delta v_T \\ \delta v_N \end{bmatrix} = \begin{bmatrix} \delta v \cos \psi \\ \delta v \sin \psi \\ 0 \end{bmatrix} \qquad (43)$$

where δv is the magnitude of the impulse velocity increment $\delta \boldsymbol{v}$, ψ is the direction angle of the impulse maneuver which is in the orbital plane, and the definition of ψ is shown in Fig. 2.

5. Filter design

The inter-satellite separation range between the space target and the chaser spacecraft is assumed to be much smaller than the relative range between the chaser spacecraft and the center of the earth. Simplifying the nonlinear differential equation of the relative dynamics to linear differential equation as

$$\dot{\boldsymbol{x}}(t) = \boldsymbol{A}(t)\boldsymbol{x}(t) + \boldsymbol{\Gamma}(t)\delta \boldsymbol{v}(t) \qquad (44)$$

where $\boldsymbol{A}$ denotes the vectors of the relative dynamics of the system.

The solution of the linear differential equation can be represented by the state transition matrix $\boldsymbol{\Phi}$. The state and measurement equations in the presence of external control-input and measurement uncertainty are obtained as

$$\begin{cases} \boldsymbol{x}(t) = \boldsymbol{\Phi}(t,t_0)\boldsymbol{x}(t_0) + \int_{t_0}^{t} \boldsymbol{\Phi}(t,\mu)\boldsymbol{\Gamma}(\mu)\delta \boldsymbol{v}(\mu)\mathrm{d}\mu \\ \boldsymbol{z}(t) = \boldsymbol{H}(t)\boldsymbol{x}(t) + \boldsymbol{\zeta}(t) \end{cases} \qquad (45)$$

where $\boldsymbol{\zeta}$ denotes the measurement errors is characterized by a normal distribution with zero mean and covariance $\boldsymbol{R} = \mathrm{E}[\boldsymbol{\zeta}\boldsymbol{\zeta}^\mathrm{T}] = \mathrm{diag}(\sigma_\alpha^2, \sigma_\varepsilon^2)$, and $\boldsymbol{H}$ is the partial derivative of the LoS measurements $\boldsymbol{z}$ with respect to the estimation state $\boldsymbol{x}$.

The partial derivative $\boldsymbol{H}$ is calculated by applying the following chain rule [31]:

$$\boldsymbol{H}(t) = \frac{\partial \boldsymbol{z}}{\partial \delta \bar{\alpha}}\bigg|\delta \bar{\alpha} =$$

$$\frac{\partial \boldsymbol{z}}{\partial \boldsymbol{r}_{\mathrm{rel}}} \cdot \frac{\partial \boldsymbol{r}_{\mathrm{rel}}}{\partial \boldsymbol{r}^{\mathrm{J2000}}} \cdot \frac{\partial \boldsymbol{r}^{\mathrm{J2000}}}{\partial \boldsymbol{r}^{\mathrm{RTN}}} \cdot \frac{\partial \boldsymbol{r}^{\mathrm{RTN}}}{\partial \delta \bar{\alpha}}\bigg|\delta \bar{\alpha} =$$

$$\left(\frac{\partial \alpha}{\partial \boldsymbol{r}_{\mathrm{rel}}} \cdot \frac{\partial \varepsilon}{\partial \boldsymbol{r}_{\mathrm{rel}}}\right)^\mathrm{T} \cdot \boldsymbol{R}_{\mathrm{J2000}}^c \cdot \boldsymbol{R}_{\mathrm{RTN}}^{\mathrm{J2000}} \cdot \frac{\partial \boldsymbol{r}^{\mathrm{RTN}}}{\partial \delta \bar{\alpha}}\bigg|\delta \bar{\alpha} \qquad (46)$$

where $\boldsymbol{R}_{\mathrm{J2000}}^c$ is the rotation matrix from the J2000 inertial frame to the camera frame, $\boldsymbol{R}_{\mathrm{RTN}}^{\mathrm{J2000}}$ is the rotation matrix from the local Cartesian orbital frame to the J2000 inertial frame.

The following linear model is used to give the mapping between the ROEs and the relative position vector $\boldsymbol{r}^{\mathrm{RTN}}$ depicted in the local Cartesian orbital frame

$$\frac{\partial \boldsymbol{r}^{\mathrm{RTN}}}{\partial \delta \bar{\alpha}}\bigg|\delta \bar{\alpha} =$$

$$\begin{pmatrix} 1 & 0 & -\cos u & -\sin u & 0 & 0 \\ 0 & 1 & 2\sin u & -2\cos u & 0 & 0 \\ 0 & 0 & 0 & 0 & \sin u & -\cos u \end{pmatrix}. \qquad (47)$$

The measurements partials with respect to the relative position vector $\boldsymbol{r}_{\mathrm{rel}}$ depicted in the camera frame can be computed using the following equivalence [32]:

$$\frac{\partial \boldsymbol{r}_{\mathrm{rel}}}{\partial \boldsymbol{r}_{\mathrm{rel}}} = \boldsymbol{I}_{3\times 3} = \boldsymbol{\rho}^c \frac{\partial r}{\partial \boldsymbol{r}_{\mathrm{rel}}} + r\frac{\partial \boldsymbol{\rho}^c}{\partial \alpha}\frac{\partial \alpha}{\partial \boldsymbol{r}_{\mathrm{rel}}} + r\frac{\partial \boldsymbol{\rho}^c}{\partial \varepsilon}\frac{\partial \varepsilon}{\partial \boldsymbol{r}_{\mathrm{rel}}} \qquad (48)$$

where $r = \|\boldsymbol{r}_{\mathrm{rel}}\|$ and $\boldsymbol{\rho}^c = \dfrac{\boldsymbol{r}_{\mathrm{rel}}}{\|\boldsymbol{r}_{\mathrm{rel}}\|}$, $\dfrac{\partial \boldsymbol{\rho}^c}{\partial \alpha}$ and $\dfrac{\partial \boldsymbol{\rho}^c}{\partial \varepsilon}$ are expressed as

$$\begin{cases} \dfrac{\partial \boldsymbol{\rho}^c}{\partial \alpha} = \begin{pmatrix} \cos \alpha \cos \varepsilon \\ 0 \\ -\cos \varepsilon \sin \alpha \end{pmatrix} \\ \dfrac{\partial \boldsymbol{\rho}^c}{\partial \varepsilon} = \begin{pmatrix} -\sin \varepsilon \sin \alpha \\ \cos \varepsilon \\ -\sin \varepsilon \cos \alpha \end{pmatrix} \end{cases}. \qquad (49)$$

The partial derivatives of the azimuth α and elevation ε with respect to the relative position vector $\boldsymbol{r}_{\mathrm{rel}}$ depicted in the camera frame can be calculated by alternately multiplying $\left(\dfrac{\partial \boldsymbol{\rho}^c}{\partial \alpha}\right)^\mathrm{T}$ and $\left(\dfrac{\partial \boldsymbol{\rho}^c}{\partial \varepsilon}\right)^\mathrm{T}$ by (48):

$$\begin{cases} \dfrac{\partial \alpha}{\partial \boldsymbol{r}_{\mathrm{rel}}}\bigg|\delta \bar{\alpha} = \dfrac{1}{r\cos^2(\varepsilon)}\left(\dfrac{\partial \boldsymbol{\rho}^c}{\partial \alpha}\right)^\mathrm{T} \\ \dfrac{\partial \varepsilon}{\partial \boldsymbol{r}_{\mathrm{rel}}}\bigg|\delta \bar{\alpha} = \dfrac{1}{r}\left(\dfrac{\partial \boldsymbol{\rho}^c}{\partial \varepsilon}\right)^\mathrm{T} \end{cases}. \qquad (50)$$

The dynamic filter is designed based on extended Kalman filter (EKF), which includes one-step prediction equations

$$\begin{cases} \hat{\boldsymbol{x}}_{k|k-1} = \boldsymbol{f}(\hat{\boldsymbol{x}}_{k-1}, \delta \boldsymbol{v}_{k-1}) \\ \boldsymbol{P}_{k|k-1} = \boldsymbol{F}(\hat{\boldsymbol{x}}_{k-1})\boldsymbol{P}_{k-1}\boldsymbol{F}^\mathrm{T}(\hat{\boldsymbol{x}}_{k-1}) + \boldsymbol{G}_{k-1}\boldsymbol{Q}_{k-1}\boldsymbol{G}_{k-1}^\mathrm{T} \end{cases} \qquad (51)$$

where $\boldsymbol{F}$ denotes the Jacobian matrix of $\boldsymbol{f}$ with respect to the estimation state $\boldsymbol{x}$, $\boldsymbol{G}$ denotes the distribution matrix of process noise, $\boldsymbol{Q}$ denotes the process noise covariance matrix, and $\boldsymbol{P}_{k|k-1}$ denotes the prediction error covariance matrix.

Update equations:

$$\begin{cases} \boldsymbol{K}_k = \boldsymbol{P}_{k|k-1}\boldsymbol{H}_k^\mathrm{T}(\boldsymbol{H}_k\boldsymbol{P}_{k|k-1}\boldsymbol{H}_k^\mathrm{T} + \boldsymbol{R}_k)^{-1} \\ \hat{\boldsymbol{x}}_k = \hat{\boldsymbol{x}}_{k|k-1} + \boldsymbol{K}_k(\boldsymbol{z}_k - \boldsymbol{H}_k\hat{\boldsymbol{x}}_{k|k-1}) \\ \boldsymbol{P}_k = (\boldsymbol{I} - \boldsymbol{K}_k\boldsymbol{H}_k)\boldsymbol{P}_{k|k-1} \end{cases} \qquad (52)$$

where $\boldsymbol{K}$ is the filter gain, $\boldsymbol{P}_k$ is the estimation error covariance matrix.

6. Simulation validation

6.1 Semi-physical simulation system

A semi-physical simulation system is built to verify the proposed optimal maneuver strategy, which is shown in

Fig. 4 and Fig. 5. The semi-physical simulation system is equipped with a three-axis linear guide and a three-axis turntable, which can adjust the star map display and the camera to be coaxial.
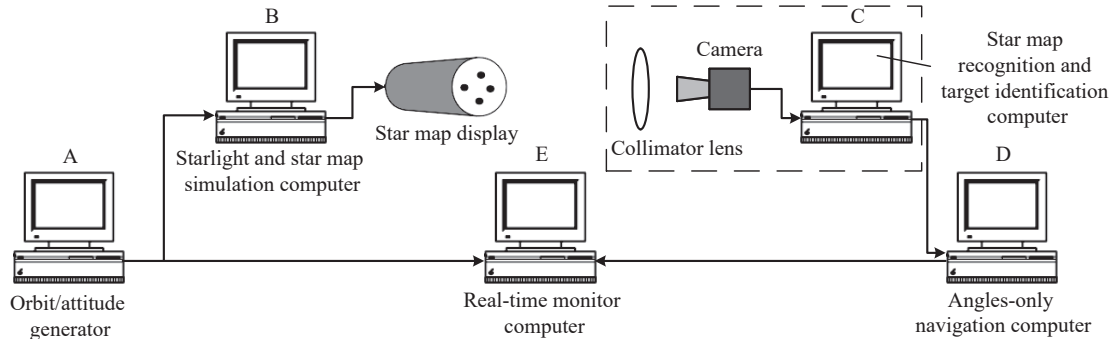

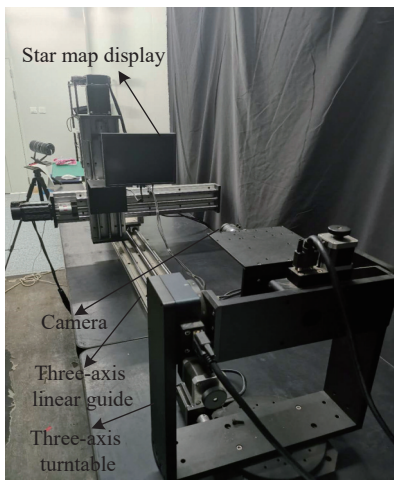**Fig. 4   Block diagram of semi-physical simulation system**

Fig. 5   Semi-physical simulation system

The key components of the semi-physical simulation system include:

(i) Orbit/attitude generator: the module is equipped with Matlab/simulink and Satellite Tool Kitl (STK) software, which are used to generate the relative trajectories between the chaser spacecraft and the space target.

(ii) Starlight and star map simulation computer: as a starlight and star map simulator, the computer is used to simulate the distribution and magnitude of the stars in the star map.

(iii) Star map recognition and target identification computer: the computer is used to find the space target in the star map and output the LoS measurements of the space target relative to the camera frame.

(iv) Angles-only navigation computer: the computer is used to accomplish the real-time calculation of the angles-only navigation algorithms and output the filtering results.

(v) Real-time monitoring computer: the computer is used to display and monitor the attitude/orbit parameters of the chaser spacecraft and the space target, as well as the filtering results of the angles-only navigation algorithms.

6.2   Numerical analysis and experimental verification

For the need of the experimental verification, the theoretical relative motion state of the space target relative to the chaser spacecraft is numerically propagated using a 20×20 gravity field and including J_2 perturbations, solar radiation pressure, third-body and atmospheric drag perturbations. A set of LoS observations is finally created from the theoretical relative motion state. The experimental verification is mainly carried out in three typical relative orbital scenarios, and the relative trajectories are shown in Fig. 6, including ROE1 which represents a possible configuration for the beginning of an approach to an space target; ROE2 which presents a drift of almost 1 km per orbit toward an space target; ROE3 which represents the starting point of a docking phase. The main simulation parameters are shown in Table 1.
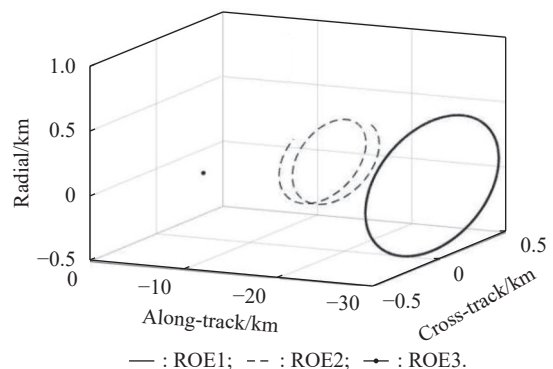

— : ROE1;   -- : ROE2;   → : ROE3.

Fig. 6   Relative trajectories in three typical orbital scenarios

Table 1   Main simulation parameters

Parameter	Value
Absolute orbital elements of the space target (a/km, e, i/(°), Ω/(°), ω/(°), M/(°))	(6 878.137, 0, 40, 120, 0, 50)
ROE1 ($a\delta a$, $a\delta\lambda$, $a\delta e_x$, $a\delta e_y$, $a\delta i_x$, $a\delta i_y$)/km	(0, −30, 0.5, 0, −0.5, 0)
ROE2 ($a\delta a$, $a\delta\lambda$, $a\delta e_x$, $a\delta e_y$, $a\delta i_x$, $a\delta i_y$)/km	(−0.15, −20, 0.3, 0, −0.3, 0)
ROE3 ($a\delta a$, $a\delta\lambda$, $a\delta e_x$, $a\delta e_y$, $a\delta i_x$, $a\delta i_y$)/km	(0, −5, 0, 0, 0, 0)
Sample period T/s	10
Simulation time t_f/s	1 000
Sensor measurement noise ($\sigma_\alpha = \sigma_\varepsilon$)/arcsec	30

When the maximum magnitude $\upsilon=1$ m/s of the impulse velocity increment δv, according to (41), the optimal maneuver schemes in three typical orbital scenarios are given as

ROE1:

$$(\delta v)_{obj} = [-0.976\ 1, 0.217\ 1, 0.009\ 5]^T\text{m/s};$$

ROE2:

$$(\delta v)_{obj} = [-0.974\ 0, 0.226\ 2, 0.008\ 4]^T\text{m/s};$$

ROE3:

$$(\delta v)_{obj} = [-0.974\ 5, 0.224\ 4, -0.003\ 0]^T\text{m/s}.$$

The values of the objective function J under different maneuver schemes in three typical orbital scenarios are shown in Fig. 7, including no maneuver, the maneuver which is out of the orbital plane, the maneuvers which are in the orbital plane (i.e., the direction angle ψ are 0°, 45° and 90°, respectively), and the optimal maneuver. The relative trajectories are shown in Fig. 8. It can be seen from Fig. 7 that the values of the objective function J under the optimal maneuver strategy proposed in this paper are smaller than that in other cases, which proves the validity of the analytical solution of the optimal maneuver strategy proposed in this paper. In addition, it is not that the impulse maneuver performed by the chaser spacecraft will definitely improve the observability of angles-only navigation. When the direction angle ψ of the impulse maneuver in the orbital plane are 0° and 45°, the values of the objective function J are larger than that when there is no maneuver. Hence the chaser spacecraft must perform the impulse maneuver in a certain direction to improve the observability of angles-only navigation.

— : No maneuver; - - - : Out-of-plane; ····· : ψ=0°; — : ψ=45°; – - : ψ=90°; ······ : Optimal.
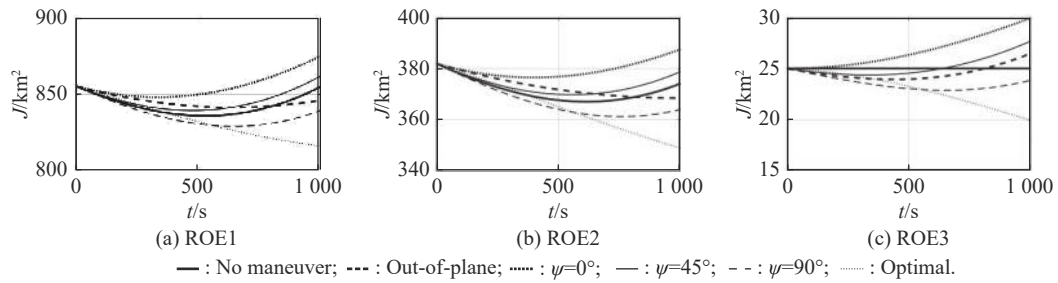
Fig. 7   Values of the objective function J evolving over time

— : No maneuver; - - - : Out-of-plane; ····· : ψ=0°; — : ψ=45°; – - : ψ=90°; ······ : Optimal.
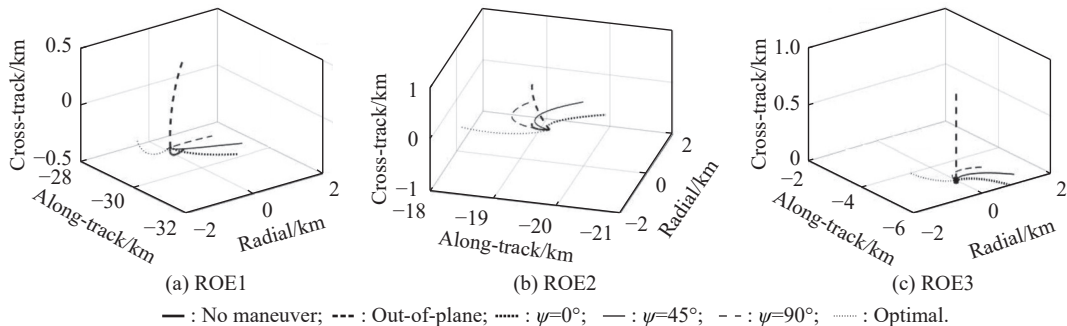
Fig. 8   Relative trajectories under different maneuver schemes

The azimuth α and the elevation ε of the space target relative to the chaser spacecraft before and after the optimal impulse maneuver in three typical orbital scenarios are shown in Fig. 9. The absolute values of the difference of the azimuth α and the elevation ε (i.e., $|\alpha_m - \alpha|$ and $|\varepsilon_m - \varepsilon|$) before and after the optimal impulse maneuver in three typical orbital scenarios are shown in Fig. 10. It can be seen from Fig. 9 and Fig. 10 that the change in the ele-

vation ε is greater than the change in the azimuth α before and after the optimal impulse maneuver. Hence the observability of angles-only navigation can be effectively improved by increasing the change in the elevation ε before and after the impulse maneuver. In addition, the absolute values of the difference of the elevation ε in ROE3 are greater than that in ROE1 and ROE2 before and after the optimal impulse maneuver.

(a) Azimuth α in ROE1   (b) Elevation ε in ROE1   (c) Azimuth α in ROE2

(d) Elevation ε in ROE2   (e) Azimuth α in ROE3   (f) Elevation ε in ROE3
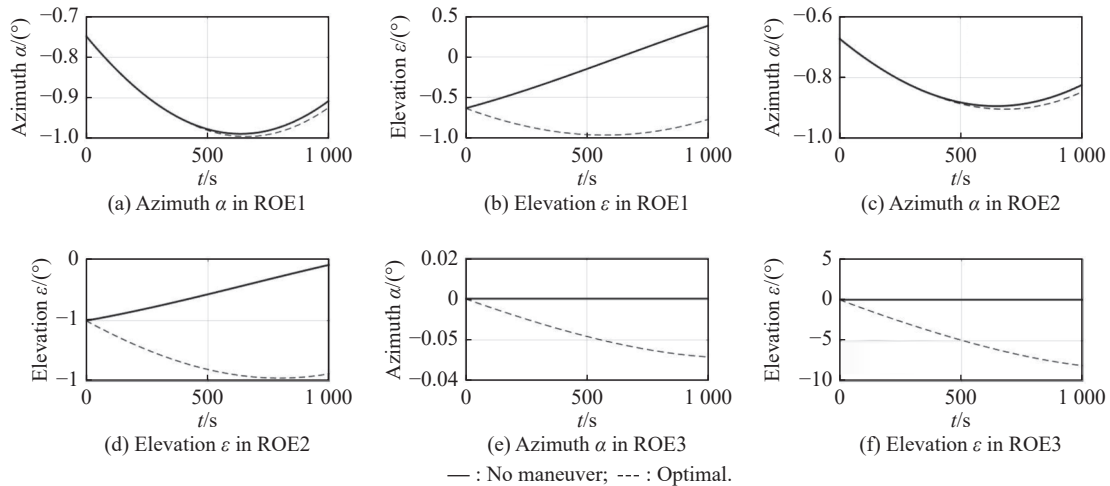
— : No maneuver; --- : Optimal.

Fig. 9 Azimuth and elevation of the space target relative to the chaser spacecraft before and after the optimal impulse maneuver

(a) Absolute values of the difference of the azimuth α in ROE1

(b) Absolute values of the difference of the elevation ε in ROE1

(c) Absolute values of the difference of the azimuth α in ROE2

(d) Absolute values of the difference of the elevation ε in ROE2

(e) Absolute values of the difference of the azimuth α in ROE3

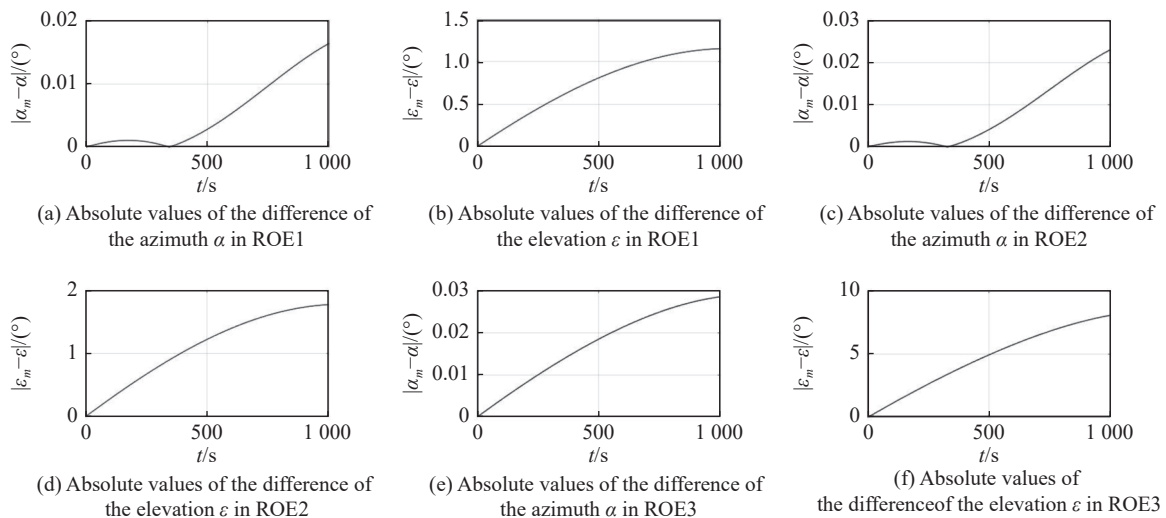(f) Absolute values of the difference of the elevation ε in ROE3

Fig. 10 Absolute values of the difference of the azimuth and the elevation before and after the optimal impulse maneuver

Finally, the performances of the angles-only navigation filter under different maneuver schemes in three typical orbital scenarios are compared, and the results are shown in Fig. 11−Fig. 13. It can be seen from Fig. 11−Fig. 13 that the optimal maneuver strategy proposed in this paper can significantly reduce the errors of the relative position of the angles-only navigation filter in the

radial, tangential, and normal directions. Compared with the cases without orbital maneuver, it is concluded that the tangential filtering accuracy with the optimal orbital maneuver at the terminal time is increased by 35% on average, and the radial and normal filtering accuracy is increased by 30% on average. In addition, not all maneuver schemes in any directions can improve the perfor-

mances of the angles-only navigation filter, and the chaser spacecraft must perform the impulse maneuver in a certain direction to improve the performances of the angles-only navigation filter. The results obtained here further prove the validity of the analytical solution of the optimal maneuver strategy proposed in this paper, which is consistent with the above analysis of the values of the objective function J under different maneuver schemes.
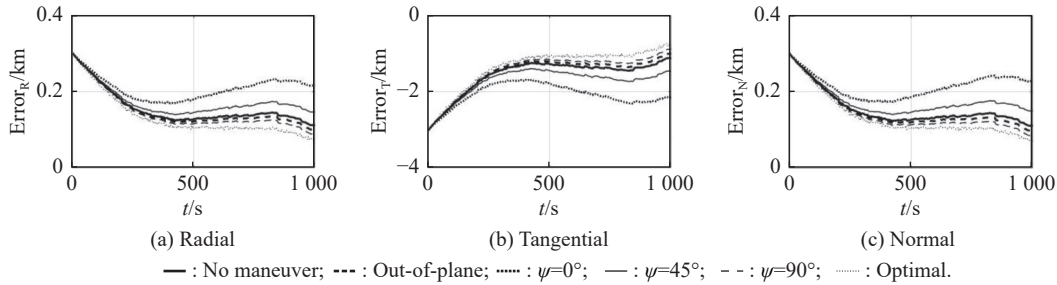

— : No maneuver; --- : Out-of-plane; ⋯⋯ : $\psi=0°$;　— : $\psi=45°$;　- - : $\psi=90°$;　⋯⋯ : Optimal.

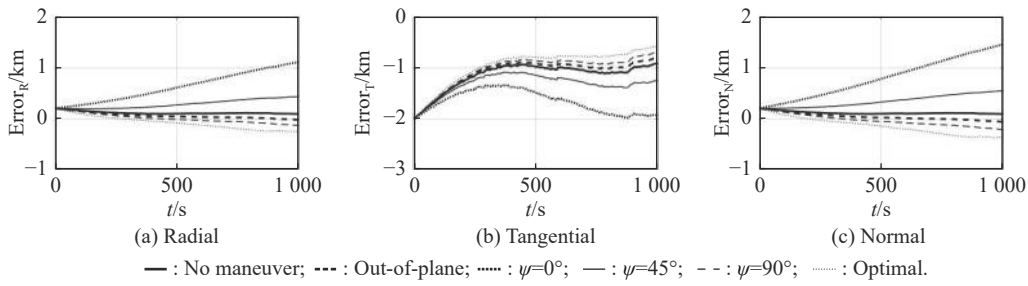**Fig. 11　Errors of the relative position of the angles-only navigation filter under different maneuver schemes in ROE1**

— : No maneuver; --- : Out-of-plane; ⋯⋯ : $\psi=0°$;　— : $\psi=45°$;　- - : $\psi=90°$;　⋯⋯ : Optimal.

Fig. 12　Errors of the relative position of the angles-only navigation filter under different maneuver schemes in ROE2

— : No maneuver; --- : Out-of-plane; ⋯⋯ : $\psi=0°$;　— : $\psi=45°$;　- - : $\psi=90°$;　⋯⋯ : Optimal.
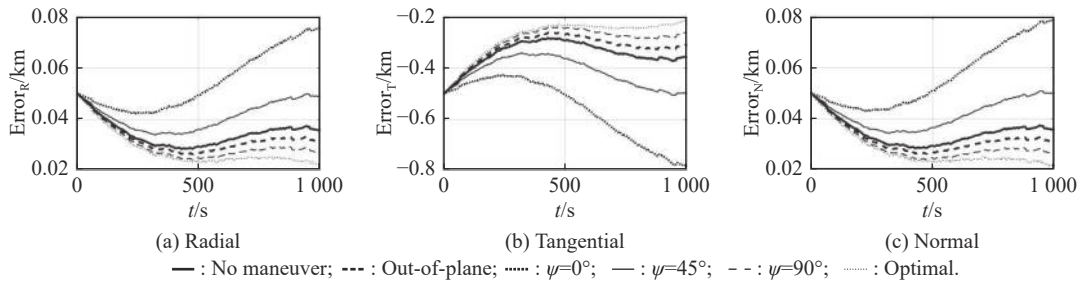
Fig. 13　Errors of the relative position of the angles-only navigation filter under different maneuver schemes in ROE3

7. Conclusions

This paper proposes an optimal maneuver strategy to improve the observability of angles-only rendezvous from the perspective of relative navigation. The analytical solution of the optimal maneuver strategy to improve the observability of angles-only navigation by means of numerical analysis is obtained. A set of semi-physical simulation system is built to verify the optimal maneuver strategy proposed in this paper. The effectiveness of the optimal maneuver strategy proposed in this paper is verified by comparing the objective function of the observability of angles-only navigation and the performances of the angles-only navigation filter in three typical orbital

scenarios. This optimal maneuver strategy can not only improve the observability of angles-only navigation, but also reduce the errors of the relative position of the angles-only navigation filter in the radial, tangential and normal directions, and its performances are better than other maneuver schemes. Compared with the cases without orbital maneuver, it is concluded that the tangential filtering accuracy with the optimal orbital maneuver at the terminal time is increased by 35% on average, and the radial and normal filtering accuracy is increased by 30% on average.

The optimal maneuver strategy proposed in this paper to improve the observability of angles-only rendezvous does not consider various constraints such as the field of

view of the optical camera and the safety trajectory, and only the cases of the single-impulse maneuver are analyzed. In the future, it is necessary to study the optimal maneuver strategy to improve the observability of angles-only rendezvous in orbital scenarios with various constraints and considering multi-impulse maneuver or continuous low-thrust maneuver, so as to further expand its practicability.

References

[1] SEARS P J, HO J. Impact evaluation of in-space additive manufacturing and recycling technologies for on-orbit servicing. Journal of Spacecraft and Rockets, 2018, 55(4): 1498–1508.

[2] CHIU S W. Promoting international cooperation in the age of global space governance: a study on on-orbit servicing operations. Acta Astronautica, 2019, 161: 375–381.

[3] RAZZAGHI P, KHATIB E A, BAKHTIARI S. Sliding mode and SDRE control laws on a tethered satellite system to de-orbit space debris. Advances in Space Research, 2019, 64(1): 18–27.

[4] CHU Z Y, WEI T, SHEN T, et al. Optimal commands based multi-stage drag de-orbit design for a tethered system during large space debris removal. Acta Astronautica, 2019, 163: 238–249.

[5] ZHU Z H, GUO Y. Adaptive coordinated attitude control for spacecraft formation with saturating actuators and unknown inertia. Journal of the Franklin Institute, 2019, 356: 1021–1037.

[6] IVANOV D, KUSHNIRUK M, OVCHINNIKOV M. Study of satellite formation flying control using differential lift and drag. Acta Astronautica, 2018, 152: 88–100.

[7] MITCHELL A, PIMENTA D, GILL J, et al. Cardiovascular effects of space radiation: implications for future human deep space exploration. European Journal of Preventive Cardiology, 2019, 26(16): 1707–1714.

[8] LI H, ZHANG Q Y, ZHANG N T. Autonomous navigation of formation flying spacecrafts in deep space exploration and communication by hybrid navigation utilizing neural network filter. Acta Astronautica, 2009, 65: 1028–1031.

[9] HAN J, LI W X, FENG K, et al. Vision-based aerial image mosaicking algorithm with object detection. Journal of Systems Engineering and Electronics, 2022, 33(2): 259–268.

[10] GONG B C, LI W D, LI S, et al. Angles-only initial relative orbit determination algorithm for non-cooperative spacecraft proximity operations. Astrodynamics, 2018, 2: 217–231.

[11] GAIAS G, ARDAENS J S. Flight demonstration of autonomous non-cooperative rendezvous in low earth orbit. Journal of Guidance, Control and Dynamics, 2018, 41: 1137–1154.

[12] D'AMICO S, PAVONE M, SARAF S, et al. Miniaturized autonomous distributed space systems for future science and exploration. Proc. of the 8th International Workshop of Spacecraft Formation Flying, 2015. https://elib.dlr.de/98200/.

[13] GELLER D K, PEREZ A C. Initial relative orbit determination for close-in proximity operations. Journal of Guidance, Control and Dynamics, 2015, 38: 1833–1841.

[14] GRZYMISCH J, FICHTER W. Observability criteria and unobservable maneuvers for in-orbit bearings-only navigation. Journal of Guidance, Control and Dynamics, 2014, 37(4): 1250–1259.

[15] GRZYMISCH J, FICHTER W. Optimal rendezvous guidance with enhanced bearings-only observability. Journal of Guidance, Control and Dynamics, 2015, 38(6): 1131–1139.

[16] GELLER D K, KLEIN I. Angles-only navigation state observability during orbital proximity operations. Journal of Guidance, Control and Dynamics, 2014, 37(6): 1976–1983.

[17] NEWMAN B, LOVELL T A, PRATT E, et al. Quadratic hexa-dimensional solution for relative orbit determination. Proc. of the AIAA/AAS Astrodynamics Specialist Conference, 2014. https://www.webofscience.com/wos/alldb/full-record/wos:00371647200201.

[18] PEREZ A C, GELLER D K, LOVELL T A. Non-iterative angles-only initial relative orbit determination with J_2 perturbations. Acta Astronautica, 2018, 151: 146–159.

[19] WOFFINDEN D C, GELLER D K. Observability criteria for angles-only navigation. IEEE Trans. on Aerospace and Electronic System, 2009, 45(3): 1194–1208.

[20] ARDAENS J S, GAIAS G. A numerical approach to the problem of angles-only initial relative orbit determination in low earth orbit. Advances in Space Research, 2019, 63(12): 3884–3899.

[21] ROSCOE C, WESTPHAL J, GRIESBACH J, et al. Formation establishment and reconfiguration using differential elements in J_2-perturbed orbits. Journal of Guidance, Control and Dynamics, 2015, 38(9): 1725–1740.

[22] GAIAS G, D'AMICO S, ARDAENS J S. Generalized multi-impulsive maneuvers for optimum spacecraft rendezvous in near-circular orbit. International Journal of Space Science and Engineering, 2015, 3(1): 68–88.

[23] CHERNICK M, D'AMICO S. New closed-form solutions for optimal impulsive control of spacecraft relative motion. Journal of Guidance, Control, and Dynamics, 2018, 41(2): 301–319.

[24] KOENIG A, GUFFANTI T, D'AMICO S. New state transition matrices for relative motion of spacecraft formations in perturbed orbits. Proc. of the AIAA/AAS Astrodynamics Specialist Conference, 2016: 1749−1768.

[25] GAIAS G, ARDAENS J S, MONTENBRUCK O. Model of J_2 perturbed satellite relative motion with time-varying differential drag. Celestial Mechanics and Dynamical Astronomy, 2015, 123(4): 411–433.

[26] VADDI S, ALFRIEND K, VADALI S, et al. Formation establishment and reconfiguration using impulsive control. Journal of Guidance, Control and Dynamics, 2005, 28(2): 262–268.

[27] GRZYMISCH J, FICHTER W. Analytic optimal observability maneuvers for in-orbit bearings-only rendezvous. Journal of Guidance, Control and Dynamics, 2014, 37(5): 1658–1664.

[28] DAVIS C. Theory of positive linear dependence. American Journal of Mathematics, 1954, 76(4): 733–746.

[29] BOYD S, VANDENBERGHE L. Convex optimization. Cambridgeshire: Cambridge University Press, 2004.

[30] YIN J F, HAN C. Elliptical formation control based on relative orbit elements. Chinese Journal of Aeronautics, 2013, 26: 1554–1567.

[31] GAIAS G, D'AMICO S, ARDAENS J S. Angles-only navigation to a non-cooperative satellite using relative orbital elements. Journal of Guidance, Control and Dynamics, 2014, 37(2): 439–451.

[32] BATTIN R H. An introduction to the mathematics and methods of astrodynamics. Reston: American Institute of Aeronautics & Astronsutics, 1999.

Biographies

DU Ronghua was born in 1995. He received his B.S. degree in mechanical engineering from the School of Mechanical Engineering, Nanjing University of Science and Technology, Nanjing, China, in 2017. He is pursuing his Ph.D. degree in mechanical engineering from the School of Mechanical Engineering, Nanjing University of Science and Technology, Nanjing, China. Since 2017, he has studied in the the Micro Satellite Research Centre and has been a postgraduate with the School of Mechanical Engineering, Nanjing University of Science and Technology, Nanjing, China. His research interests include satellite attitude determination, vision-based relative navigation, guidance navigation and control, and angles-only relative navigation.

E-mail: Duronghua1995@126.com

LIAO Wenhe was born in 1965. He received his B.S. degree in aerospace manufacturing engineering from the School of Mechanical and Electrical Engineering, Nanjing University of Aeronautics and Astronautics, Nanjing, China, in 1990 and Ph.D. degree in aerospace manufacturing engineering from the School of Mechanical and Electrical Engineering, Nanjing University of Aeronautics and Astronautics, Nanjing, China, in 1996. He is currently the Vice President of the Nanjing University of Science and Technology, Nanjing, China. He is also the Director of the Micro Satellite Research Centre and a professor with the School of Mechanical Engineering, Nanjing University of Science and Technology, Nanjing, China. His research interests include satellite system design and high-end equipment design.

E-mail: cnwho@mail.njust.edu.cn

ZHANG Xiang was born in 1973. He received his B.S. degree in aerospace manufacturing engineering from the School of Mechanical and Electrical Engineering, Nanjing University of Aeronautics and Astronautics, Nanjing, China, in 1998 and Ph.D. degree in aerospace manufacturing engineering from the School of Mechanical and Electrical Engineering, Nanjing University of Aeronautics and Astronautics, Nanjing, China, in 2007. He is currently the Deputy Director of the Micro Satellite Research Centre and a professor with the School of Mechanical Engineering, Nanjing University of Science and Technology, Nanjing, China. His research interests include satellite system design, satellite attitude control, satellite payloads, and ground stations.

E-mail: zhxiang2002@126.com